Hydrothermal deposition on the Juan de Fuca Ridge over multiple glacial–interglacial cycles

Kassandra M. Costa [a,b,*], Jerry F. McManus [a,b], Jennifer L. Middleton [c,d], Charles H. Langmuir [c], Peter J. Huybers [c], Gisela Winckler [a,b], Sujoy Mukhopadhyay [d]

[a] *Lamont-Doherty Earth Observatory of Columbia University, Palisades, NY 10964, USA*
[b] *Department of Earth and Environmental Sciences, Columbia University, New York, NY 10027, USA*
[c] *Department of Earth and Planetary Sciences, Harvard University, Cambridge, MA 02138, USA*
[d] *Department of Earth and Planetary Sciences, University of California Davis, Davis, CA 95616, USA*

A B S T R A C T

Hydrothermal systems play an important role in modern marine chemistry, but little is known about how they may have varied on 100,000 year timescales. Here we present high-resolution records of non-lithogenic metal fluxes within sediment cores covering the last 500,000 years of hydrothermal deposition on the flanks of the Juan de Fuca Ridge. Six adjacent, gridded cores were analyzed by x-ray fluorescence for Fe, Mn, and Cu concentrations, corrected for lithogenic inputs with Ti, and normalized to excess initial ^{230}Th to generate non-lithogenic metal flux records that provide the longest orbitally resolved reconstructions of hydrothermal activity currently available. Fe fluxes vary with global sea level over the last two glacial cycles, suggesting higher hydrothermal deposition during interglacial periods. The observed negative relationship between Fe and Mn indicates variable sediment redox conditions and diagenetic remobilization of sedimentary Mn over time. Thus, Mn fluxes may not be a reliable indicator for hydrothermal activity in the Juan de Fuca Ridge sediment cores. Cu fluxes show substantial high-frequency variability that may be linked to changes in vent temperature related to increased magmatic production during glacial periods. Deglacial hydrothermal peaks on the Juan de Fuca Ridge are consistent with previously published records from the Mid-Atlantic Ridge and the East Pacific Rise. Moreover, on the Juan de Fuca Ridge, the deglacial peaks in hydrothermal activity are followed by relatively high hydrothermal fluxes throughout the ensuing interglacial periods relative to the previous glacial period.

© 2017 Elsevier B.V. All rights reserved.

1. Introduction

Hydrothermal vents are unique biogeochemical environments in the deep ocean. More than a hundred modern hydrothermal systems have been discovered, in every ocean, at both divergent and convergent tectonic margins (e.g., Beaulieu et al., 2013). Despite their importance to the marine environment, however, little is known about how hydrothermal systems and their chemical fluxes may fluctuate and evolve over long timescales. Long-term (million-year) studies (e.g., Kuhn et al., 2000; Lyle et al., 1986) have demonstrated that hydrothermal activity responds to major tectonic events, such as spreading jumps and ridge reorganization, but these records do not have the resolution to investigate hydrothermal variability on orbital (10s–100s kyr) timescales. Reconstructions at higher resolution are critical for investigating the nascent

hypothesis that glacial–interglacial sea level variability may influence mid-ocean ridge (MOR) systems. Lowering of global sea level during glacial periods would reduce the hydrostatic pressure on mid-ocean ridge melt centers (Huybers and Langmuir, 2009; Lund and Asimow, 2011), inducing an increase in melt production that might also generate vigorous hydrothermal venting and thicker ocean crust. Milankovitch cycles in ocean ridge bathymetry have been observed at the Southern East Pacific Rise (Tolstoy, 2015) and in the Australian–Antarctica Ridge (Crowley et al., 2015), but their relationship to climate remains contentious (Huybers et al., 2016; Olive et al., 2016a, 2016b, 2015; Tolstoy, 2016). Reconstructions of hydrothermal activity on the Mid-Atlantic Ridge (Middleton et al., 2016) and the East Pacific Rise (Lund et al., 2016; Lund and Asimow, 2011) reveal pulses of hydrothermal activity, but whether this phenomenon is globally representative and consistent across longer glacial–interglacial timescales as well as prior deglaciations remains unknown.

Furthermore, the integrity of metal fluxes as a proxy for hydrothermal activity has yet to be scrutinized with regards to
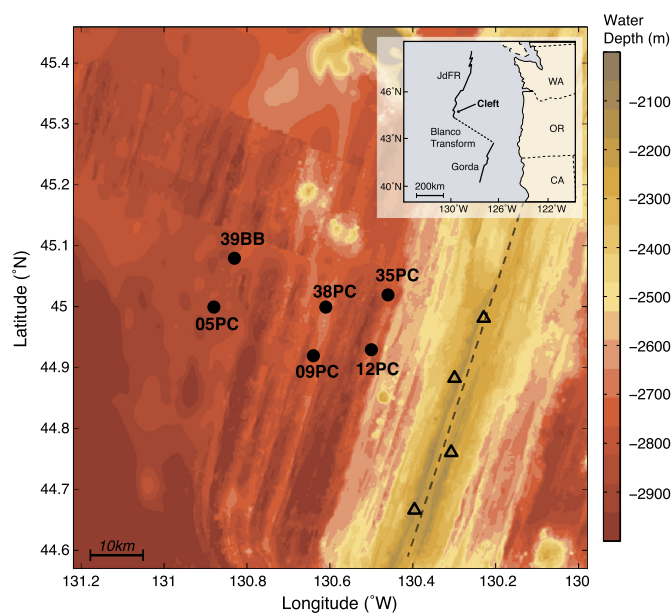
Fig. 1. Map of the study region. Bathymetric map of the Cleft Segment, with inset showing the geographic position of the Juan de Fuca Ridge in the Northeast Pacific Ocean. The ridge can be identified as the NE–SW trending bathymetric high (in yellow), and the axis is identified with a dashed line. AT26-19 core locations on the western flank of the ridge are shown with black dots. Triangles show the locations of known modern hydrothermal vents (Beaulieu et al., 2013). (For interpretation of the references to color in this figure legend, the reader is referred to the web version of this article.)

the elemental variability of hydrothermal chemistry at a mid-ocean ridge. Distinct chemical signatures in different hydrothermal sources can create ambiguity in interpreting trends in metal fluxes in ridge flank sediments. While modern vent systems appear to be relatively stable in terms of vent dynamics and plume chemistry over observational timescales (years to decades), these plume characteristics may not maintain stability over longer time periods (1,000s to 10,000s years). In this paper, we utilize a gridded suite of sediment cores on the Juan de Fuca Ridge to reconstruct elemental fluxes of Fe, Mn, and Cu in order to evaluate how hydrothermal activity has varied over multiple glacial cycles.

2. Materials & methods

2.1. Regional setting and core sites

The Juan de Fuca Ridge (JdFR) is located in the Northeast Pacific Ocean about 500 km off the coast of North America, and the Cleft Segment study area comprises the southern end of the JdFR system (Fig. 1). This intermediate spreading ridge (56 mm/yr; Wilson, 1993) is characterized by extensive hydrothermal activity and hot spot volcanism (Karsten and Delaney, 1989; Massoth et al., 1994; Normark et al., 1983). Modern hydrothermal activity on the Cleft Segment occurs within the axial cleft in hydrothermal fields at the north and south ends of the segment (Baker, 1994; Embley and Chadwick, 1994; Massoth et al., 1994). Typical plumes from these vents precipitate hydrothermal particles rich in Fe, Mn, and Cu (Feely et al., 1994), which have been observed as far as 100 km away from the ridge (Baker et al., 1985). Major eruptive events in the 1980s generated new pillow mounds and reinvigorated hydrothermal activity along the segment (Embley and Chadwick, 1994), and these observations are consistent with the expectation that hydrothermal activity may respond to increased magmatic activity (Baker and Hammond, 1992).

This study focuses on the long, stratigraphically intact records of six sediment cores (AT26-19-05PC, -09PC, -12PC, -35PC, -38PC,

-39BB) collected on the SeaVOICE cruise of the R/V Atlantis in September 2014 to the JdFR (44.89–44.97°N, 130.50–130.88°W, 2678–2711 m). The cores form two transects extending west of the ridge, with 05PC and 39BB the farthest from the ridge (∼50 km), then 09PC and 38PC (28 km) and 12PC and 35PC as the closest to the ridge (18 km) (Fig. 1). Despite repeated attempts, cores were not recovered east of the ridge, possibly because the east side of the ridge is covered in a basalt flow that may be impenetrable to standard coring procedures. Age models for the sediment cores have been developed using benthic $\delta^{18}O$, coretop radiocarbon, and lithologic stratigraphy (Costa et al., 2016). The region exhibits highly variable sedimentation patterns, both spatially and temporally, with a large range of sedimentation rates (0.25–3.18 cm/kyr). Compositionally, the sediments show clear glacial–interglacial variations in dry bulk density (Costa et al., 2016) and mass flux (Costa and McManus, 2017) that largely reflect carbonate preservation cycles.

2.2. Analytical methodology for metal concentrations

Cu, Fe, Mn, and Ti intensities (count rates) were measured with an XRF core scanner (ITRAX, Cox Ltd., Sweden) at Lamont-Doherty Earth Observatory of Columbia University (LDEO). Split core surfaces were smoothed and covered with ChemPlex Proline transmission film to minimize desiccation during analysis. XRF was performed at 2 mm resolution, using an integration time of 2 s and a molybdenum x-ray source set to 30 kV and 45 mA. Several cores (05PC, 09PC, and 12PC) were measured with a similar XRF core scanner (ITRAX, Cox Ltd., Sweden) at Woods Hole Oceanographic Institution. Those analyses were performed at 4 mm resolution, using an integration time of 10 s and a molybdenum x-ray source set to 30 kV and 45 mA. Results are comparable between the two instruments and indicate high reproducibility in the XRF measurements (Supplementary Fig. 1). Data from the LDEO scans will be used throughout this paper to remain consistent between the six cores.

XRF intensities were calibrated using discrete measurements analyzed by flux fusion. Samples from 05PC, 09PC, and 12PC were selected to cover the full range of XRF intensities observed in each core, and Cu, Fe, Mn, and Ti concentrations were analyzed by flux fusion following the procedure of Murray et al. (2000). Dried, homogenized samples (100 ± 5 mg) were combined with lithium metaborate flux (400 ± 10 mg) in graphite crucibles and fused at 1050 °C for 8–10 min. The graphite crucibles were removed from the furnace and agitated to ensure aggregation of the fused material. After reheating to 1050 °C, the fused bead was dissolved in 10% HNO_3, agitated for approximately 10 min, and then filtered and diluted for analysis. Samples were analyzed on an Agilent 720 Inductively Coupled Plasma Optical Emission Spectrometer (ICP-OES) at LDEO, and ICP-OES intensity data were calibrated to concentrations with fluxed standard reference materials (JLS-1, JDO-1, SCO-1, AGV-2, DTS-2b, W-2a) (Supplementary Fig. 2). Relative standard deviations are based on ten total replicates of the VOICE internal megastandard (VIMS): ±6.2% for Cu, ±2.0% for Fe, ±3.6% for Mn, and ±1.8% for Ti. Flux fusion data are provided in Supplementary Table 1.

Empirical calibrations of the XRF data were generated by iterative reduced major axis (RMA) regression of the XRF intensities and discrete elemental data (Rousseau et al., 1996). The XRF records were smoothed at 1 cm scale and interpolated onto the depths of the discrete samples, and an initial RMA regression was performed. Outliers were identified as those data points greater than five standard deviations away from the initial regression. A second RMA regression was then recalculated on the dataset with the outliers removed. Overall the XRF and ICP data agree reasonably well ($r^2 = 0.88$ for Cu, $r^2 = 0.92$ for Fe, $r^2 = 0.87$ for Mn,

$r^2 = 0.86$ for Ti; $p < 0.001$) (Supplementary Fig. 3), providing a robust calibration for the high-resolution XRF records. As no inter-core discrepancies were apparent, the same calibration was applied to all six cores. Calibrated XRF data are provided in Supplementary Table 2.

2.3. Lithogenic correction

High sedimentary metal concentrations may be diagnostic of hydrothermal activity, but non-hydrothermal materials such as ae-olian dust and continental sediments also supply metals to marine sediment. The total metal concentrations will vary with both hy-drothermal activity and lithogenic inputs, and therefore it is imper-ative to quantify and remove the lithogenic fraction of each metal before interpreting any authentic hydrothermal signal. Ti is almost entirely derived from the lithogenic fraction (Murray et al., 1993), in contrast to Al, which can be enriched in hydrothermal fluids (Resing et al., 2015; Shimmield and Price, 1988; Von Damm et al., 1985). Multiplying Ti by the average ratio of upper continental crust (e.g., Fe/Ti of 11.7 wt%/wt%, Taylor and McLennan, 1995) con-strains the lithogenic metal contributions. Once the lithogenic con-centration is subtracted from the total concentration, the residual is interpreted as hydrothermal. We designate lithogenic-corrected metal concentrations as Fe_H, Mn_H, and Cu_H (Fig. 2, Supplementary Figs. 4 and 5).

While, the actual Fe/Ti ratio of lithogenic material in the JdFR sediments may not equal the presumed ratio of 11.7, an offset in the composition of the lithogenic endmember would not sig-nificantly alter the temporal trends observed in the hydrothermal flux records. All potential lithogenic source materials to the JdFR sediments contain Fe/Ti ratios that are lower than the average ra-tio of upper continental crust, including Asian dust (average ∼11, Ferrat et al., 2011), Pacific pelagic sediments (10–11, Goldberg and Arrhenius, 1958; Kyte et al., 1993), mid-ocean ridge basalts (8, Dixon et al., 1986), sediments from the Cascadia Subduction Zone (10.2, Plank, 2014), and sediments from the Columbia River (av-erage ∼6.7, Whetten et al., 1969; White, 1970). The Fe/Ti ratio of 10.7–11.5 within the regionally occurring turbidite layer (Costa et al., 2016) may be representative of the lithogenic endmember in the JdFR sediment cores. Given these possibilities, the hydrother-mal fraction calculated using the lithogenic ratio of 11.7 likely rep-resents a minimum estimate that nevertheless reveals the persis-tence of hydrothermal deposition on JdFR. Adjusting the lithogenic endmember to a constant but lower value would increase apparent hydrothermal fluxes, possibly erroneously, but would not signifi-cantly alter the reconstructed temporal variability (Supplementary Fig. 6A). In some cases, where there is independent evidence for high basalt contributions to the sediment, as near the base of the one study core that reached basement (Ferguson et al., 2017), us-ing lithogenic Fe/Ti of 11.7 overestimates the amount of lithogenic Fe in the sediment. While a lower Fe/Ti closer to 8 may be ap-propriate in these limited intervals, we prefer to employ the single value of 11.7 to maintain consistency between all six cores.

Changes in the lithogenic endmember over time (e.g. from glacial to interglacial periods) could also affect the temporal vari-ability in hydrothermal reconstruction. For example, lithogenic Fe/Ti might be high (∼12) during glacial periods, when global dust fluxes are high (e.g., Winckler et al., 2008), and lower (∼8) dur-ing interglacial periods. However, these relatively small changes in lithogenic Fe/Ti ratios are likely to have minimal impact on the hy-drothermal records and would only serve to exaggerate the glacial–interglacial trends observed on the JdFR (Supplementary Fig. 6c). The alternative variability, in which lithogenic composition varies such that lithogenic Fe/Ti values were lower (∼8) during glacial periods and higher (∼12) during interglacial periods, would damp the glacial–interglacial cycles and result in a generally more con-
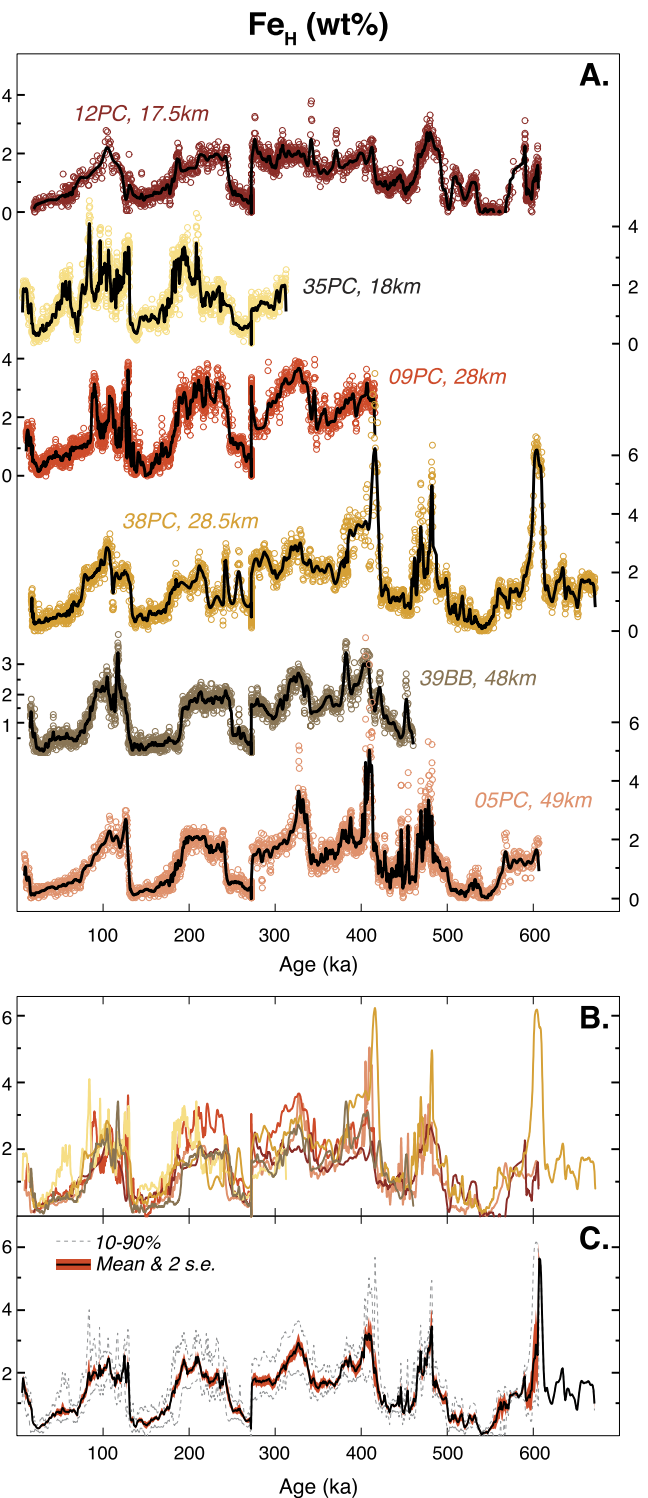
Fig. 2. Compilation of individual iron records into a regional stack. Records have been corrected for lithogenic inputs using titanium (Methods Section 2.3). Cores are ordered according to their current distance from the ridge (A), from the closest (12PC, 17.5 km) to the farthest away (05PC, 49 km). Circles represent the individual high-resolution XRF datapoints, while the solid black lines are the data smoothed with a 20-pt hamming filter. Despite traversing over 30 km, the mean Fe_H concen-trations seem to be independent of distance from the ridge, which is consistent with long-lived particulate iron concentrations in hydrothermal plumes (Fitzsimmons et al., 2017). Over the last 300 ka, for which data from all 6 cores are available, mean Fe_H concentrations are 1.1 wt% at 18 km, 1.2 wt% at 28 km, and 1.1 wt% at 49 km. The coherency between the six records is even more apparent when they are over-lain (B) and then stacked (C) as demonstrated by the narrow 2 standard error window (red shading in C). Dashed lines show the 10–90% range of all six records. Comparable figures for Mn and Cu are provided in Supplementary Figs. 3–4.

stant hydrothermal iron flux (Supplementary Fig. 6b). At this time, we do not have enough information to prefer a variable lithogenic endmember (Supplementary Figs. 6b and 6c) over a constant endmember (Supplementary Fig. 6a), and so we simply employ a constant endmember ratio of 11.7 wt%/wt% to limit the addition of further unknowns. Future work on lithogenic sources using additional provenance proxies (e.g., ^{4}He/^{232}Th, Winckler et al., 2008) may better quantify the variability in lithogenic endmembers in this region. The main conclusions of this paper are not substantially altered by variations in Fe/Ti ratios within the known range (8–12).

2.4. Calculation of metal fluxes using the constant flux proxy ^{230}Th

In addition to lithogenic dilution of hydrothermal metal deposition, hydrothermal material can also be diluted by bulk sedimentary components, such as calcium carbonate and non-hydrothermal silicate. An increase in the relative concentration (wt%) of Fe_H may be due to increased hydrothermal deposition, but it could just as easily result from a decreased concentration of calcium carbonate. Correcting for calcium carbonate dilution (e.g. carbonate-free-basis concentrations) does not account for the dilution effects of changes in the concentrations of opal and terrestrial material. The constant flux proxy method is able to accommodate these complexities and provide a clear measure of hydrothermal input. Relative elemental concentrations (wt%, or g/g) are converted to absolute elemental fluxes (g/cm^2 kyr) by multiplying by the particle flux (also referred to as bulk mass flux or mass accumulation rate). To generate core-specific flux records (see Section 3), XRF data were smoothed at 1 cm scale and then interpolated onto the depths of the discrete ^{230}Th mass flux samples (Costa and McManus, 2017). These fluxes monitor the absolute input from the hydrothermal source, and thus they are more sensitive to changes in hydrothermal activity than relative concentration proxies that only describe how hydrothermal inputs compare with carbonate or detrital inputs.

Particle flux can be calculated using constant flux proxies (^{230}Th and ^{3}He) or by using more traditional mass accumulation rates based on age models. Constant flux proxies offer two distinct advantages over the age-model based approach 1) higher resolution (Bacon, 1984; Francois et al., 2004) and 2) insensitivity to sediment focusing, which can be particularly variable on the rough bathymetry of mid-ocean ridges (Costa and McManus, 2017). As a result, constant flux proxies provide regionally homogeneous calculations of particle fluxes (Costa and McManus, 2017; Kienast et al., 2007; Ruhlemann et al., 1996) despite the variability in sedimentation rates prevalent at scales of tens-of-kilometers (Costa et al., 2016; Johnson and Johnson, 1970). In this study, we employ excess initial ^{230}Th (^{230}Th$_{xs}$^{0}, hereafter simply ^{230}Th) as a constant flux proxy, a widely used approach in paleoceanographic studies (for example: Frank et al., 1995; Jacobel et al., 2017; McManus et al., 1998; Thomson et al., 1993; Winckler et al., 2008). The basis of this approach is that ^{234}U is highly soluble in seawater but decays to relatively insoluble ^{230}Th at a constant rate in the water column. Virtually all ^{230}Th produced in the water column is rapidly scavenged by settling particles, and its concentration in sediments is thus inversely dependent on the particle flux. See the review by Francois et al. (2004) for more on this proxy and Costa and McManus (2017) for its utility on the Juan de Fuca Ridge.

Moreover, reexamination of ^{230}Th data from hydrothermal settings indicates that the utility of ^{230}Th as a constant flux proxy is not disturbed by hydrothermal scavenging, although this has been previously suggested (Feely et al., 1990; Frank et al., 1994; German et al., 2002, 1997, 1991; Lund and Asimow, 2011; Shimmield and Price, 1988). Enhanced scavenging of ^{230}Th has been attributed to both hydrothermal Fe (German et al., 1991) and Mn (Frank et al., 1994) particles, largely due to an observed positive correlation between these metals and ^{230}Th concentrations in mid-ocean ridge sediment. However, these correlations do not necessarily represent a causal relationship: the simultaneous variability in ^{230}Th and Fe (or Mn) concentrations can be attributed to dilution by changes in calcium carbonate burial. In fact, on the JdFR no relationship between ^{230}Th and Fe (or Mn) concentrations remains when their concentrations are presented on a carbonate free basis (Supplementary Fig. 7). Carbonate dilution similarly explains the relationship between ^{230}Th and Fe on the Galapagos Microplate (Frank et al., 1994) (Supplementary Fig. 7). Although increased scavenging of rare earth elements, oxyanions, and U-series nuclides may occur in the hydrothermal plume, especially close (<1 km) to the vent site (Feely et al., 1990; Frank et al., 1994; German et al., 2002, 1997, 1991; Shimmield and Price, 1988), our results demonstrate that these effects do not appear in far field sediments (>10 km). This is consistent with recent water column observations showing that hydrothermal particles scavenge excess ^{230}Th at the vent site, but with increasing distance from the ridge, ingrowth from uranium decay and reversible exchange with seawater reproduce ^{230}Th fluxes to the sediment that are consistent with the production rate in the full water column (Pavia et al., 2017). Thus, ^{230}Th provides a suitable tool to investigate particle fluxes in hydrothermal areas.

The applicability of ^{230}Th normalization is opportune given the order of magnitude variability in sedimentation rates (Costa et al., 2016) caused by sediment focusing along the rough bathymetry of mid-ocean ridges (Costa and McManus, 2017). Under these conditions, age-model based particle flux calculations will overestimate the hydrothermal deposition during time periods when sediment focusing is high, because this calculation does not take into account the lateral input of sediment (Francois et al., 2004). Consequentially the two methods of normalization generate different records of hydrothermal history, both in trend and amplitude. For example, using the same iron concentrations but normalizing with age-model based mass accumulation rates (Lund et al., 2016) or ^{230}Th (Frank et al., 1994) affects both when and how large the deglacial peak in hydrothermal flux occurs on the Galapagos Microplate (Supplementary Fig. 8). In this study, we will only interpret hydrothermal records that are normalized to constant flux proxies. We compare the ^{230}Th-normalized JdFR records presented here to a ^{3}He normalized hydrothermal record from the TAG site (Middleton et al., 2016), two ^{230}Th normalized hydrothermal records from the Galapagos Microplate (Frank et al., 1994), and two ^{3}He normalized hydrothermal records from the East Pacific Rise (Lund et al., 2016).

3. Spatial variability on the JdFR

The gridded suite of cores utilized in this study presents a unique dataset for investigating the spatial variability of hydrothermal deposition on ridge flanks. Hydrothermal fluxes are unlikely to be spatially uniform, but instead they will vary with both plume trajectory and vent location. Plume trajectories shift with deep sea currents, and hydrothermal vent locations migrate along the ridge over timescales of thousands to tens of thousands of years (Baker, 1994). While modern vent locations and plumes can easily be mapped, the spatial parameters of paleo-venting and paleo-plumes are unknown. These previously unconstrained spatial effects could generate ambiguity when interpreting sedimentary records, in which an increase in metal flux might reflect 1) increased hydrothermal activity (e.g., in response to lower sea level), 2) a more proximal vent location, or 3) a more direct plume trajectory.

Here we demonstrate spatial variability by assessing individual Fe_H records from the six cores on the JdFR (Fig. 3). Using a constant spreading rate and the core's modern position, Fe_H fluxes
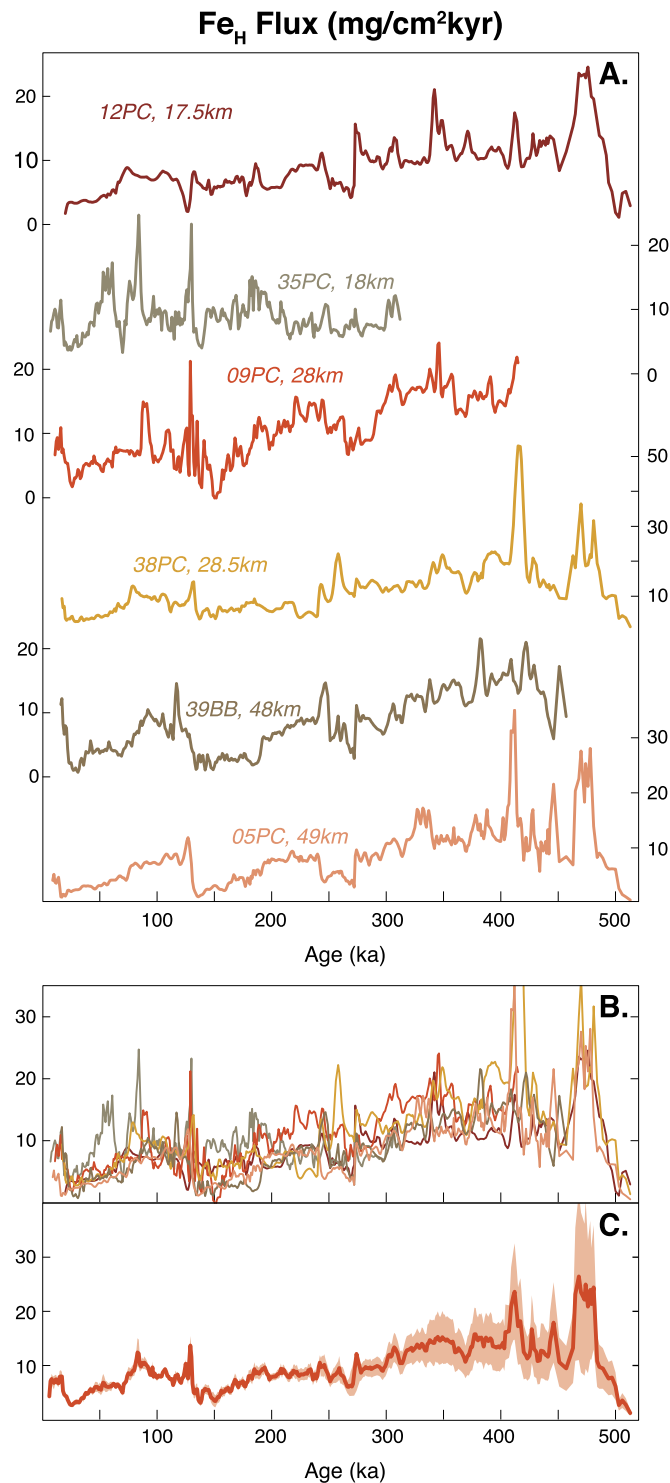
Fig. 3. Individual hydrothermal iron fluxes. Records have been corrected for lithogenic inputs using Ti (Methods Section 2.3) and normalized to ^{230}Th (Methods Section 2.4). Cores are ordered according to their current distance from the ridge (A), from the closest (12PC, 17.5 km) to the farthest away (05PC, 49 km), as in Fig. 2. Despite ranging over 30 km, the individual cores record relatively similar amplitudes of hydrothermal flux (B). The regional hydrothermal depositional history is best represented by the mean stack (C). Red envelope shows the propagated 2σ standard error, including analytical error on XRF, calibration error on XRF, and ^{230}Th mass flux error. (For interpretation of the references to color in this figure legend, the reader is referred to the web version of this article.)

can be placed in the context of proximity to the ridge (Fig. 4). These records are remarkably similar in both trend and amplitude (Fig. 3b) and do not display a pronounced decrease in flux

with increasing distance from the ridge. The lack of a distance effect is not unexpected given that the closest approach of the JdFR cores is 5 km from the ridge axis (12PC), and so they never enter the cross-axial zone of high hydrothermal iron deposition (≤5 km) (Feely et al., 1994). Averaging the fluxes over 500 kyr reveals only slightly lower values for the cores farthest from the ridge (8.0–8.2 g/cm^2 kyr; 05PC and 38PC) compared to those cores closest to the ridge (8.6–8.8 g/cm^2 kyr; 12PC and 35PC), while the mid-range cores anomalously record the highest average fluxes (10.4–11.1 g/cm^2 kyr; 09PC and 38PC). At finer spatial detail, we can compare the depositional patterns of the six cores during specific Marine Isotope Stages (MIS; Fig. 5). The Fe$_H$ flux for each core was averaged throughout each MIS and divided by the mean MIS value of the six cores. This normalization to the mean eliminates the temporal effects that influence the absolute fluxes of each time period (see Section 4.1) and allows all panels to be compared at the same scale. Notably, all six cores record Fe$_H$ fluxes within ±50% of the mean value within each MIS, and more often than not within ±20%. In the most recent MIS (2–4, 5, and 6), hydrothermal deposition is higher towards the northern transect, particularly towards 35PC. Older time periods (MIS7, 8 and 9) record hydrothermal deposition skewed more towards the southern cores, including 09PC and 12PC. MIS10 favors deposition at the intermediary cores (09PC and 38PC), while MIS11 exhibits a similar pattern to the younger time periods, but centered more prominently on 38PC. Because the JdFR cores only capture hydrothermal fluxes on the western side of the ridge, it may be injudicious to directly extrapolate shifts in deposition patterns to specific movements of plume trajectories or vent locations along the ridge axis. Yet it is clear that hydrothermal metal deposition can be variable on the scales of 10s of kilometers and 1000s of years.

This finding indicates that a single core site on the flanks of a mid-ocean ridge may not be a faithful archive of hydrothermal intensity over time. Not only is each core subject to the vagaries of spatial variability, but they are also subject to the confounding effects of bioturbation. High sedimentation rate cores (like 35PC) are able to capture high frequency hydrothermal events, whereas these features are almost entirely lost in the order of magnitude lower sedimentation rates of 12PC (Costa et al., 2016), despite its nearly identical distance from the ridge as 35PC. Only with multiple hydrothermal records can we be confident in capturing a realistic hydrothermal history of a mid-ocean ridge. One approach to resolving this issue is to combine multiple records from along different segments of a mid-ocean ridge (Lund et al., 2016). In this study, we generate elemental stacks by averaging our six records from the JdFR in order to minimize the spatial and sedimentological effects present in each individual record (Fig. 6). Hydrothermal concentrations (Fe$_H$, Mn$_H$, and Cu$_H$) were averaged (mean) within 1 kyr bins before multiplying by the ^{230}Th flux stack, also in 1 kyr bins, in order to permit the calculations of standard errors. Metal concentration and flux stacks are provided in Supplementary Table 3.

4. Stacked elemental records

Hydrothermal fluids form when seawater interacts with basaltic basement rock at high temperatures, and the chemical signature of individual plumes will vary depending on a variety of factors. The dissolved and particulate chemistry of a hydrothermal plume will be influenced by 1) the age of the hydrothermal system, 2) the volume of water flushing the basement rock, 3) the exposure time of that water to the rock substrate, 4) the temperature, pressure, and redox state of the water-rock reaction, 5) the emission temperature at the vent, 6) the composition of the basement rock (e.g. ultramafic or basaltic), 7) vapor-brine phase separation and/or admixture, and 8) mineral precipitation and settling
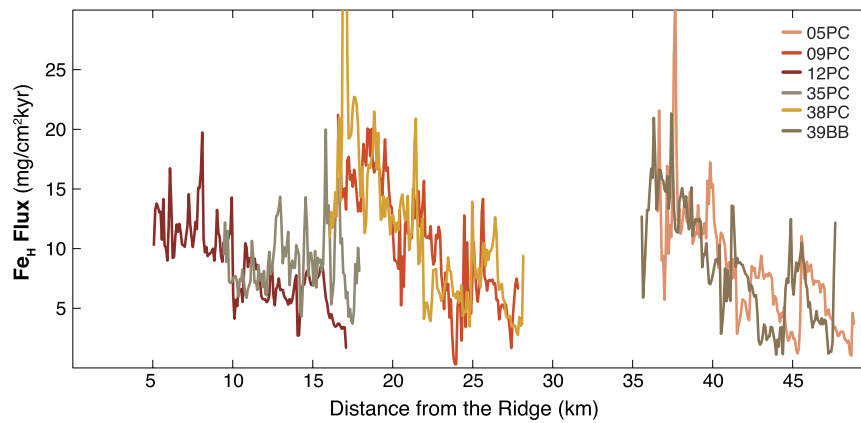
Fig. 4. Variability in hydrothermal iron fluxes with increasing distance from the ridge. Hydrothermal iron fluxes as in Fig. 3 but on a distance rather than time scale. Distance from the ridge was calculated by backtracking the core's modern position with a constant spreading rate over time. While all cores show a decline in hydrothermal iron fluxes over time, this trend is independent of distance from the ridge.
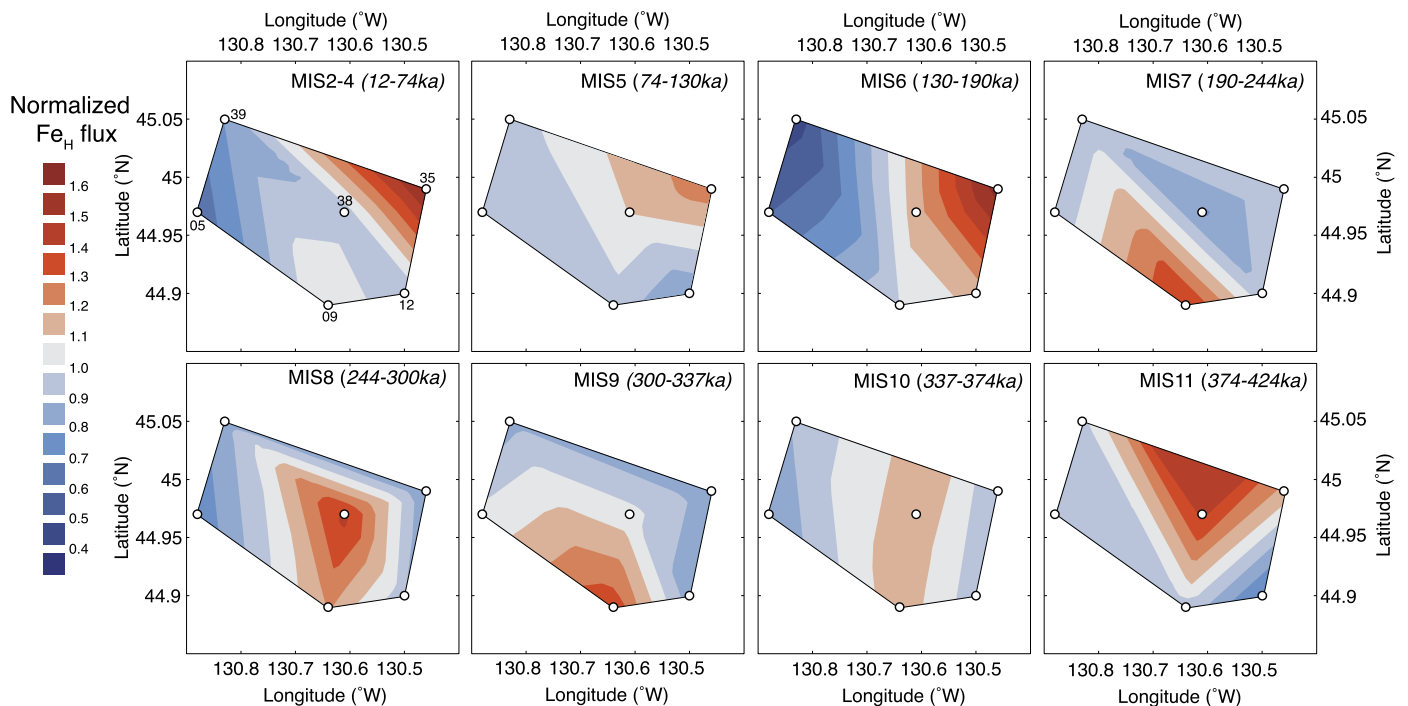

Fig. 5. Time slices of spatial deposition maps. Hydrothermal iron fluxes were averaged over the specified Marine Isotope Stage (MIS) and then normalized to the mean hydrothermal iron flux of the six cores within each time slice. Thus, a value of 1.2 indicates Fe$_H$ flux 20% greater than the average flux for that time period. Even MIS represent glacial periods, while odd MIS represent interglacial periods (e.g., Lisiecki and Raymo, 2005). Cores are labeled in the MIS2–4 panel; labels not included on other panels for clarity. Hydrothermal iron deposition often shows a bias towards the northern cores (MIS2–4, MIS5, MIS6, MIS11) and less often for the southern cores (MIS7, MIS9).

from the plume (e.g., Charlou et al., 2000; Metz and Trefry, 2000; Seyfried and Ding, 1995; Von Damm and Bischoff, 1987). Sedimentary records of hydrothermal metal fluxes can be further complicated by post-depositional diagenetic processes that can disturb the chronological reconstruction of the hydrothermal history of a ridge (e.g., Mills et al., 2010). Because different metals can be more or less sensitive to a particular process, we can leverage our three stacked elementary records (iron, manganese, and copper) to understand how hydrothermal activity on the Juan de Fuca Ridge may have varied over time.

4.1. Iron

Iron is the major chemical component of hydrothermal emissions (Edmonds and German, 2004; Feely et al., 1994, 1987), and both dissolved and particulate iron can travel in the water column over 4000 km away from the vent site (Fitzsimmons et al., 2017; Resing et al., 2015). In the buoyant plume immediately following emission, iron may form sulfides like chalcopyrite, isocubanite, and pyrite (Rudnicki, 1995; Rusakov, 2007), but sulfide precipitation ceases quickly as cold, oxygenated water is entrained into the plume (Rusakov, 2007). Estimates from the Mid-Atlantic Ridge (MAR) indicate that the iron sulfide precipitation process only results in the loss of 4% of the total vented iron concentrations from the plume to the sediment (German et al., 2010), presumably because the majority of sulfides are nanoparticulates (<100 nm) that can persist for more than two years in the water column without settling (Gartman et al., 2014; Yücel et al., 2011). Moreover, complexation with organic matter can extend the longevity of hydrothermal iron in the water column (e.g., Sander and Koschinsky, 2011), and even oxidized iron minerals can remain fixed within an organic matrix that facilitates buoyancy (Fitzsimmons et al., 2017).
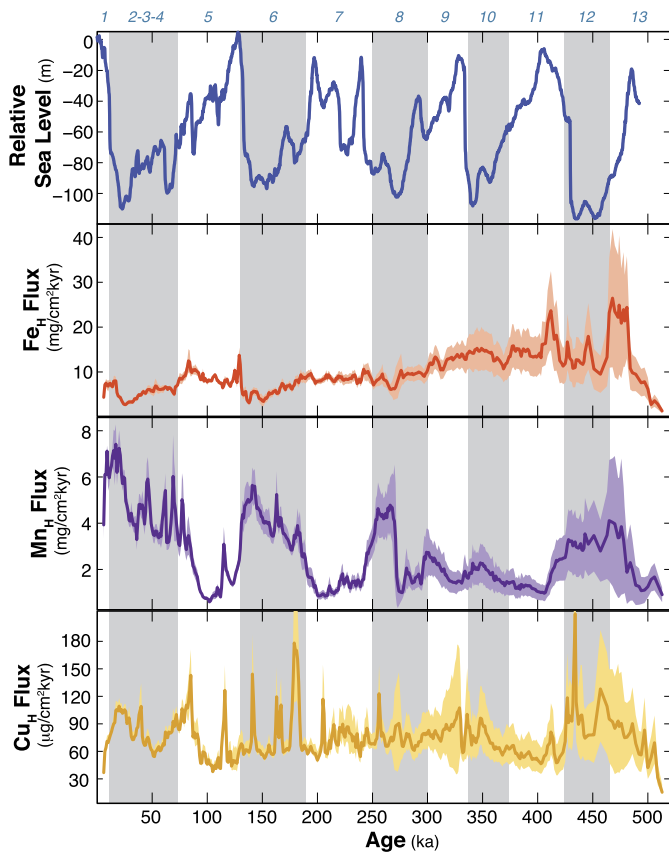
Fig. 6. Hydrothermal Fe, Mn, and Cu fluxes over the past 500 kyr. Regional metal fluxes were calculated by averaging the elemental concentrations in 1 kyr bins and then multiplying the elemental stacks by the ^{230}Th particle flux stack of Costa and McManus (2017). Marine Isotope Stages (MIS) are identified across the top of the figure with blue numbers, in which even stages (also highlighted by gray bars) indicate glacial periods. Manganese shows clearly higher fluxes during glacial periods, while iron fluxes are generally higher in interglacial periods. Copper flux is notable for its many high frequency peaks, particularly in the last 250 ka. Sea level is from Grant et al. (2014). Shaded envelopes show the propagated 2σ standard error, as in Fig. 3.

Hydrothermal iron does eventually aggregate and settle from the plume to the sediment over time, albeit several orders of magnitude more slowly than previously thought (Fitzsimmons et al., 2017), so that records of excess sedimentary iron reconstructing hydrothermal fluxes over time should be effective even at sites tens of kilometers away from the ridge.

Fe_H fluxes on the JdFR range from 1.3 mg/cm^2 kyr to 26.4 mg/cm^2 kyr, with a mean flux of 9.51 mg/cm^2 kyr (Figs. 3, 6), and hydrothermal metal deposition is persistent throughout the study interval. All sediments in all six cores display non-detrital metal fluxes, reflecting at least episodic hydrothermal activity during the centennial to millennial intervals integrated within each sample. Fe_H fluxes on the JdFR are consistent with Fe_H fluxes at other mid-ocean ridges, with higher fluxes corresponding to higher spreading rates: mean Fe_H fluxes on the JdFR are slightly higher than background fluxes at TAG on the Mid-Atlantic Ridge (1–3 mg/cm^2 kyr; Middleton et al., 2016), but lower than on the East Pacific Rise (10–12 mg/cm^2 kyr; Lund et al., 2016). Average Fe_H flux on the JdFR generally declines over time, from 13.4 mg/cm^2 kyr before 300 ka to 7.2 mg/cm^2 kyr after 300 ka. Large peaks in hydrothermal iron are also notable in the older section of the cores at 412 ka, 427 ka, 446 ka, and 465–480 ka. Flux uncertainties resulting from ^{230}Th radioactive decay in older sediments make it difficult to constrain the amplitude of these events. However future work using stable ^{3}He as a constant flux proxy will pro-

vide more insight into this potentially more episodic hydrothermal activity. In the more recent period, starting around 200 ka, Fe_H fluxes cycle between relatively high fluxes during interglacial periods (7–10 mg/cm^2 kyr) and low fluxes during glacial periods (2.5–5.5 mg/cm^2 kyr) (Fig. 6). Notably, high overall Fe_H fluxes during interglacial Marine Isotope Stage 5 (MIS5) are buttressed by abrupt Fe_H flux spikes (>12 mg/cm^2 kyr) at 83 ka and 129 ka.

The declining hydrothermal iron flux over the last 500 ka may imply that chronic hydrothermal activity may be weakening over time (Fig. 6). Linear regression indicates that hydrothermal iron flux declined at a rate of 0.0217 mg/cm^2 kyr^2 ($r^2 = 0.50$). This long-term trend may reflect the waning influence of the Cobb hotspot capture on the JdFR melting center. When the Cobb hotspot was incorporated into the JdFR around 500 ka (Desonie and Duncan, 1990; Karsten and Delaney, 1989), it stimulated increased magmatic production that generated the broad axial plateau of the Cleft segment (Carbotte et al., 2008) and caused a shift in melt composition recorded in erupted volcanic glass (Ferguson et al., 2017). Higher rates of hydrothermal activity are consistent with such a tectonically and magmatically vigorous time period. Furthermore, this general decline in hydrothermal flux is unlikely to reflect a distance related effect because it occurs at the same amplitude at all core sites, whether they moved from 5 to 15 km, 18 to 28 km, or 38 to 48 km over the course of 500 ka (Fig. 4). In contrast, a distance effect, often parameterized as a log function (e.g., Lyle et al., 1986), would have manifested as a high amplitude shift at the closest cores (12PC and 35PC) and a small to negligible shift at the 30+ km more distant cores (05PC and 39BB).

In addition to the overall decline in fluxes over time, glacial–interglacial cycling in hydrothermal iron fluxes were observed in the last 250 ka, with higher hydrothermal deposition during interglacial periods and lower hydrothermal deposition during glacial period (Fig. 6). The transition between these interglacial high and glacial low flux regimes coincided with abrupt rises in sea level associated with glacial terminations (Grant et al., 2014). The possible causative relationship between sea level and hydrothermal activity is explored in Section 5.

4.2. Manganese

Like iron, manganese is a major component of hydrothermal discharge, but unlike iron, manganese does not usually form sulfides (Von Damm et al., 1998, 1985). Oxidation of manganese occurs slowly via microbial catalyzation (Cowen et al., 1986; Dick et al., 2009; Tebo et al., 2004), and most hydrothermal manganese in a plume is present in the dissolved form: >75% near the vent and ~50% in the plume on the EPR (Fitzsimmons et al., 2017) and generally >50% on the JdFR (Feely et al., 1994; Seyfried et al., 2003) and the MAR (Charlou et al., 2000; Douville et al., 2002; Edmonds and German, 2004; Findlay et al., 2015). Models of manganese behavior within plumes corroborate low rates of particle formation (Klevenz et al., 2012). Because dissolved hydrothermal manganese concentrations tend to be stable and long-lived (Fitzsimmons et al., 2017), they are a reliable indicator for hydrothermal plumes in the water column, especially when dissolved manganese is present in a constant ratio to dissolved iron. The iron to manganese ratio is set through the interactions between seawater and basalt, which are primarily dependent on temperature, pressure, and water to rock ratio (Massoth et al., 1994; Seewald and Seyfried, 1990; Seyfried and Ding, 1995). In general, iron to manganese ratios in hydrothermal particles are slightly higher than seawater (Fe/Mn = 3.5), but they can vary over a wide range of values: Fe/Mn = 0.12–10.7 on the MAR (Charlou et al., 2000; Douville et al., 2002; German et al., 2010), Fe/Mn = 2.86–5.9
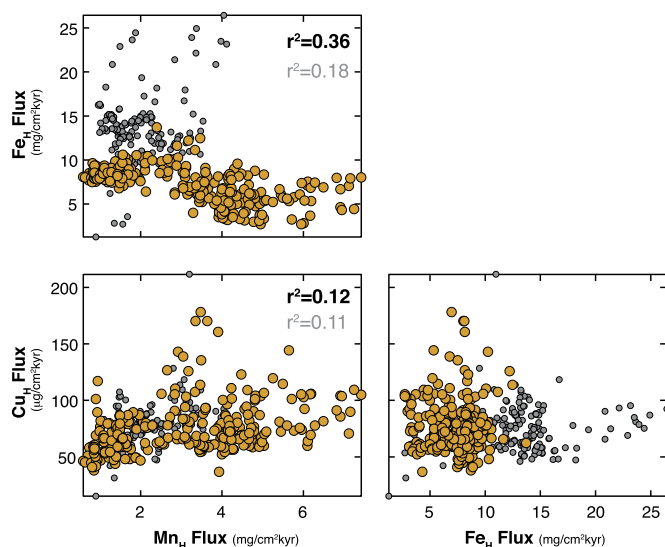
Fig. 7. Crossplots between the hydrothermal metal fluxes. Yellow dots represent data younger than 250 ka, while gray dots represent data older than 250 ka (when errors are much larger, see Fig. 6). Correlation coefficients (r^2) are provided in black for just the data younger than 250 ka and in gray for the full dataset, but only when the correlations were stronger than $r^2 = 0.10$. Weak to negligible correlations between manganese and iron and between manganese and copper suggest that the iron and copper may be more robust than manganese against post-depositional processes. (For interpretation of the references to color in this figure legend, the reader is referred to the web version of this article.)

on the EPR (Dunk and Mills, 2006; Mills et al., 2010; Schaller et al., 2000; Shimmield and Price, 1988), and Fe/Mn = 2.1–5.2 on the JdFR (Butterfield and Massoth, 1994; Seyfried et al., 2003; Von Damm and Bischoff, 1987). When iron and manganese retain a positive linear correlation in the sediment, then manganese can be comfortably interpreted as a proxy for hydrothermal activity in the past (e.g., Lund et al., 2016; Lyle et al., 1986).

In the Juan de Fuca Ridge sediments, however, iron and manganese do not demonstrate a positive linear relationship (Fig. 7). Mn_H fluxes show the clearest glacial–interglacial cycling with high fluxes during glacial periods (maximum = 7.42 mg/cm^2 kyr) and low fluxes during interglacial periods (minimum = 0.59 mg/cm^2 kyr) (Fig. 6), and the overall mean Mn_H deposition rate is 2.72 mg/cm^2 kyr. Mn_H fluxes are anticorrelated ($r^2 = 0.18$) with Fe_H fluxes (Fig. 7), and this pattern is especially pronounced in the last 250 kyr (Fig. 6). Furthermore, Mn_H fluxes appear to increase over time, particularly during glacial periods. Maximum glacial Mn_H fluxes are 4.11 mg/cm^2 kyr in MIS12 (∼465 ka), 4.78 mg/cm^2 kyr in MIS8 (∼266 ka), 5.65 mg/cm^2 kyr in MIS6 (∼141 ka), and 7.42 mg/cm^2 kyr in MIS2 (∼17 ka).

If we assume that iron and manganese are correlated in the plume, the decoupling of these two elements in the sediment must be caused by diagenetic processes, and the most likely mechanism is redox-driven remobilization of manganese (Berger et al., 1983; Dunk and Mills, 2006; Mills et al., 2010). As oxygen concentrations decrease, both manganese and iron are reduced to their more soluble forms, but the manganese transition occurs earlier than the iron transition, when oxygen concentrations are higher (Froelich et al., 1979). The extremely high Fe/Mn ratios during interglacial periods (up to 17.8) suggest at least 50% loss of plume-derived manganese to remobilization even when the hydrothermal manganese input is likely to be highest. Although a full investigation into the redox processes affecting manganese is beyond the scope of this paper, it is apparent that the manganese record on the JdFR is overprinted by diagenetic remobilization, and thus it is not a robust representation of the hydrothermal history of this

ridge. We infer the influence of diagenesis on other hydrothermal elements based on their correlation with manganese (Fig. 7). The iron record appears to have little diagenetic influence (negative correlation with manganese), and thus we interpret it as the more reliable indicator (than Mn) for hydrothermal intensity over time.

4.3. Copper

Because copper solubility is highly temperature-sensitive, its chemical behavior within hydrothermal systems may record variations in temperature of the volcanic system. Copper is more soluble at higher temperatures (Crerar and Barnes, 1976; Seewald and Seyfried, 1990; Von Damm et al., 1998), and hydrothermal fluids that are emitted at 300–400 °C will have an initial composition enriched in copper. As the fluids cool below 300–400 °C within the buoyant plume directly after emission from the vent, copper solubility rapidly decreases (Metz and Trefry, 2000; Seyfried and Ding, 1995; Trefry et al., 1994), copper sulfides like chalcopyrite will precipitate (James et al., 1995; Klevenz et al., 2012), and the residual copper concentrations within the plume will decrease (Rickard and Cowper, 1994). Vents that emit at temperatures of 300–400 °C will deposit copper-rich sulfides in the near field sediment (Feely et al., 1994; German et al., 1991; Von Damm, 1990), whereas cooler hydrothermal vents (below 300 °C) will contain very low copper concentrations from the outset. After initial copper sulfide precipitation and settling from the plume, remaining copper particulates can potentially re-dissolve and adsorb onto or incorporate into iron oxyhydroxides (Chakraborty et al., 2014; Dunk and Mills, 2006; Feely et al., 1994), possibly creating a positive relationship between iron and copper within the far-field neutrally buoyant plume (Dunk and Mills, 2006; Findlay et al., 2015). Besides temperature, hydrothermal copper concentrations in the plume can also be affected by the redox conditions of the water-rock hydrothermal reaction, in that more copper (and less iron) will be dissolved from the rock substrate under oxidizing conditions (Charlou et al., 2000; Douville et al., 2002; Seyfried and Ding, 1995; Von Damm et al., 1998).

On the Juan de Fuca Ridge, the hydrothermal copper deposition history has much greater relative variability and higher frequency than that of hydrothermal iron. Hydrothermal copper fluxes record the greatest number of high-frequency deposition events, particularly in the last 270 ka, and they range from 15.3 µg/cm^2 kyr to 212 µg/cm^2 kyr, with a mean of 75.2 µg/cm^2 kyr (Fig. 6). Copper fluxes do not show clear glacial–interglacial cycling as in manganese or iron, but instead they are characterized by numerous high amplitude (>120 µg/cm^2 kyr), high frequency pulses at ∼36 kyr intervals, particularly in the last 250 ka (Fig. 6). These peaks can sometimes be attributed to processes already identified by other elements: the copper peak at 85 ka coincides with an iron peak, indicative of increased hydrothermal fluxes at this time, and the copper peaks at 116 ka and 163 ka coincide with peaks in manganese, suggesting that those copper spikes are a result of redox-driven diagenetic remobilization. The other copper peaks (40 ka, 141 ka, 178 ka, 205 ka, 256 ka) occur independent of hydrothermal iron or manganese deposition. As described above, both temperature and redox conditions of the water-rock interaction can influence the copper fluxes in the hydrothermal plume, but because the redox conditions are largely controlled by the sulfate concentrations of seawater (Von Damm et al., 1998), they are unlikely to accommodate such high frequency variability in the hydrothermal system. Instead, we infer the high copper fluxes to be associated with higher temperature venting along the JdFR resulting in greater copper export in the plume. Most hydrothermal vents along the southern JdFR emit around the threshold for copper solubility, between 246 °C and 332 °C (Trefry et al., 1994).
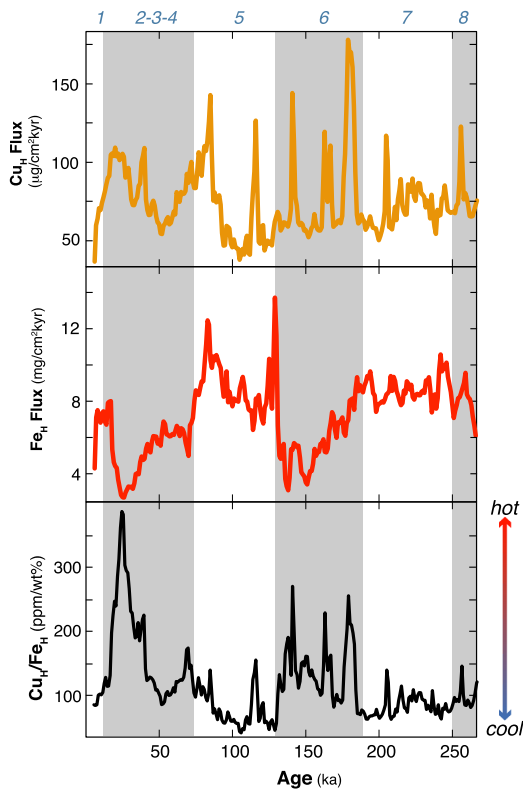
Fig. 8. Cu/Fe as an indicator for vent emission temperature. Copper fluxes are particularly sensitive to temperature, and they will be high when vent emission occurs at >300 °C (Section 4.3). Iron fluxes are not diagnostically temperature sensitive, and so higher ratios of copper to iron may be indicative of higher vent temperatures. Cu/Fe is generally higher during glacial periods, with the highest value occurring during the last glacial maximum (~20 ka). MIS are identified across the top of the figure with blue numbers, in which even stages (also highlighted by gray bars) indicate glacial periods. (For interpretation of the references to color in this figure legend, the reader is referred to the web version of this article.)

Therefore, a small increase in temperature could have a large effect on the copper concentrations by crossing the threshold into higher copper solubility in the 300–400 °C range. The incorporation of a higher temperature hydrothermal fluid has been suggested to explain higher particulate copper to iron ratios in event plumes (Butterfield et al., 1997), which are associated with increased magmatic activity (Baker et al., 1987). By extension, the high copper to iron ratios observed during glacial periods (Fig. 8) may reflect higher temperature hydrothermal activity due to increased magmatic activity and/or a shallower melt lens induced by sea level driven decompression melting (Huybers and Langmuir, 2009; Lund and Asimow, 2011).

5. Temporal reconstructions of hydrothermal activity at the JdFR, EPR, and MAR

On all three mid-ocean ridges so far investigated, hydrothermal fluxes increase at the end of the last glacial period into the deglaciation (Fig. 9). Hydrothermal iron fluxes start increasing as early as 26 ka on the Mid-Atlantic Ridge (Middleton et al., 2016), but then peak at roughly the same time: 16.8–18.9 ka on the East Pacific Rise (Lund et al., 2016), 16 ka on the Juan de Fuca Ridge, 15.5 ka on the Mid-Atlantic Ridge (Middleton et al., 2016), and 12 ka on the Galapagos (Frank et al., 1994). Age constraints are generally provided by radiocarbon dating except for the Galapagos core, which relies on planktic δ^{18}O and electron spin resonance dating for its age model (Frank et al., 1994). The youngest age constraint on the Galapagos core has an error of ±2.4 kyr based on planktic δ^{18}O and ±3.4 kyr based on electron spin resonance
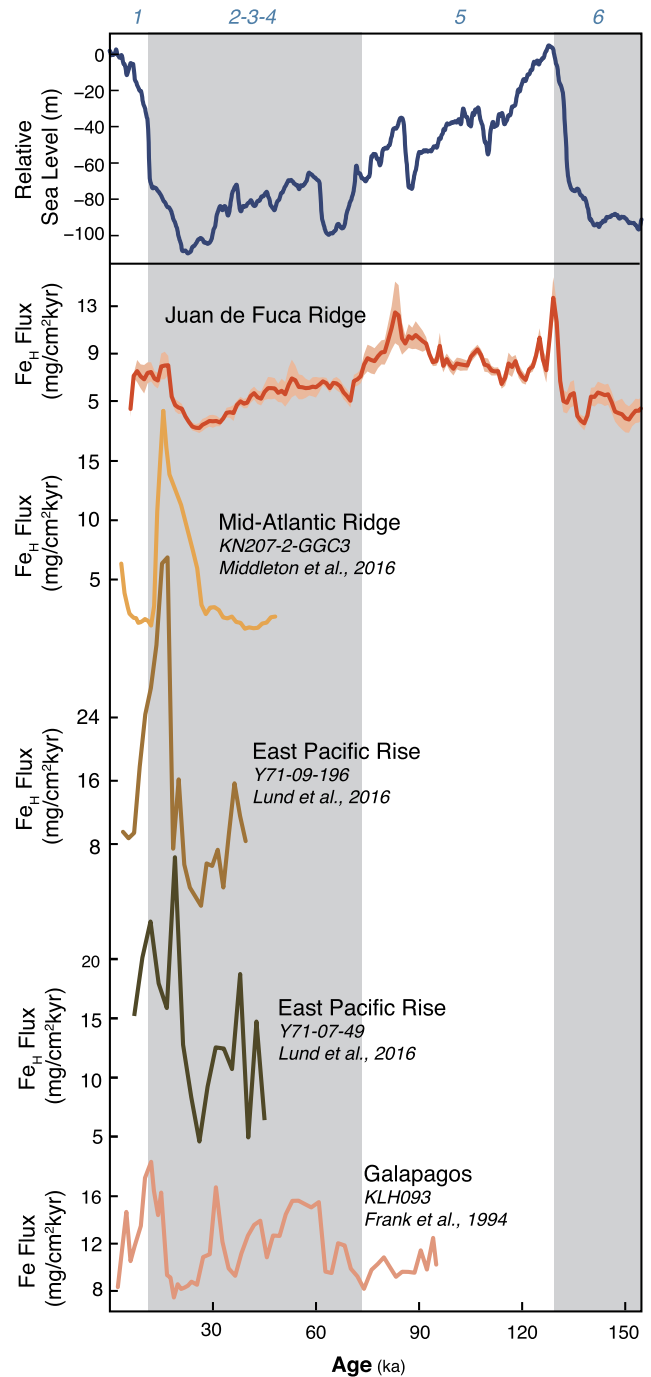
Fig. 9. Comparison with previously published hydrothermal records. Sea level from Grant et al. (2014), and MIS are identified across the top of the figure with blue numbers, in which even stages (also highlighted by gray bars) indicate glacial periods. Hydrothermal iron flux records are scaled to the same y-axis vertical dimensions. Only previously published hydrothermal records normalized to constant flux proxies (^{3}He or ^{230}Th, see Section 2.4) are included. All records show an increase in hydrothermal flux at the end of the last glacial period, between 10 and 20 ka. (For interpretation of the references to color in this figure legend, the reader is referred to the web version of this article.)

(Frank et al., 1994), and applying the upper bounds of these precision estimates would position the hydrothermal peak (15.4 ka) in line with the timing of the other records. Nominally the peak in hydrothermal activity appears to occur earliest at the fastest spreading ridge (EPR), but the apparent differences in timing are relatively small (0.5–1.8 kyr) and any true temporal offsets are difficult to resolve given confounding factors including bioturba-
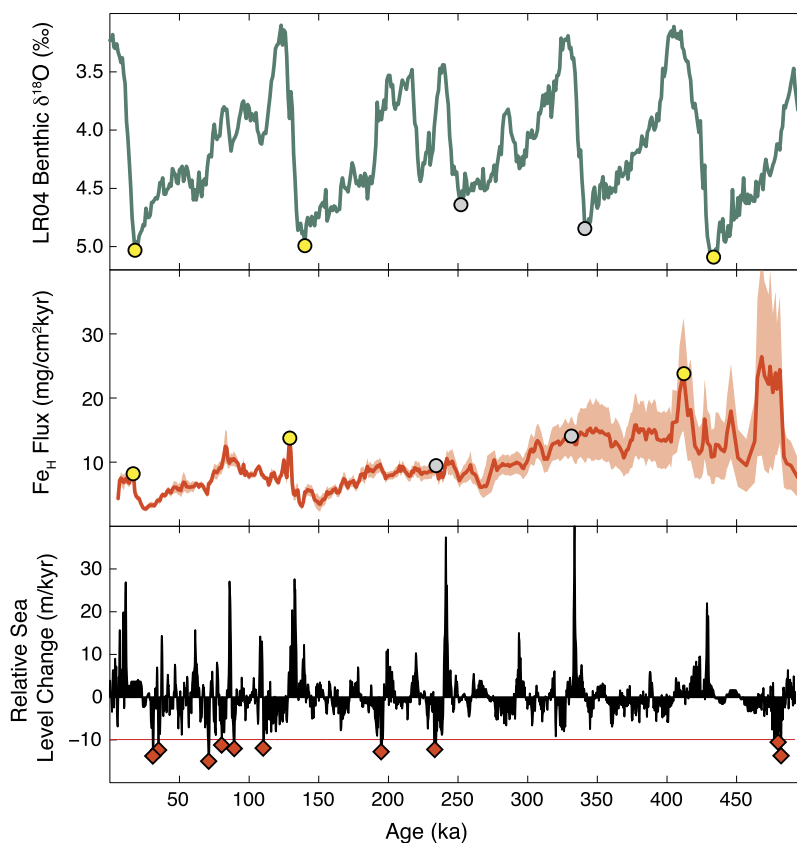
Fig. 10. Timing of hydrothermal peaks relative to changing sea level. (*Top*) Global benthic oxygen isotope stack (Lisiecki and Raymo, 2005). Higher values indicate more intense glacial periods. Glacial periods that are followed by hydrothermal peaks are highlighted by yellow dots, while those that are not followed by hydrothermal peaks are highlighted with gray dots. (*Center*) Hydrothermal Fe flux on the Juan de Fuca Ridge, as in Fig. 6. Yellow dots highlight deglaciations that contain hydrothermal peaks, while gray dots indicate deglaciations without hydrothermal peaks. (*Bottom*) Relative sea level change (Grant et al., 2014). Positive values indicate sea level rise, while negative values indicate sea level fall. Red line marks 10 m/kyr, and red diamonds highlight all sea level drops with magnitudes above the threshold for generating hydrothermal activity. (For interpretation of the references to color in this figure legend, the reader is referred to the web version of this article.)

tion, dissolution, and secondary calcification on radiocarbon dating (Mekik, 2014).

More robust are the differences in amplitude observed at the different ridges (Fig. 9). Baseline fluxes during the glacial period are calculated as the average (mean) of fluxes spanning 25 to 50 ka. The peak at JdFR corresponds to a near doubling of Fe_H flux from the baseline during the glacial period (4.5 mg/cm^2 kyr) to the hydrothermal peak (8.0 mg/cm^2 kyr). This magnitude is similar to the observed 1.6× increase on the Galapagos (11.9 to 18.9 mg/cm^2 kyr), but much lower than what is observed at either the MAR (10× increase, 1.9 to 19.2 mg/cm^2 kyr) or in two cores from the EPR (2.7× increase, 10.5 to 28.6 mg/cm^2 kyr; and 3.7× increase, 9.2 to 34.1 mg/cm^2 kyr). Both the JdFR and the Galapagos cores are located at more than 20 km from the ridge, and thus their lower amplitude Fe_H peaks may spatially integrate the hydrothermal signal from many vent sources along the ridge. The MAR core, on the other hand, is located within 1 km of the MIR hydrothermal mound within the TAG vent field (Middleton et al., 2016). The much higher amplitude of the MAR hydrothermal peak may record a near-field signal, reflecting a steep spatial gradient in the deposition of hydrothermal particles or a local signal particular to a single vent field. Thus, the 10× increase in Fe_H flux on the MAR and even the 2.7–3.7× increase in Fe_H flux on the EPR may not reflect the average change in hydrothermal flux along the global mid-ocean ridge system. Instead, the 1.5–1.6× increase in Fe_H flux, recorded at cores at greater distances (20+ km) like the JdFR, may be a more realistic representation of the magnitude of the change in hydrothermal activity witnessed by the global ocean during the deglaciation.

6. Implications for the sea level hypothesis on mid-ocean ridge systems

The similar deglacial increases in hydrothermal deposition on the JdFR, EPR, and MAR (Fig. 9) may indicate a common driving mechanism that is active on a global scale during the last two deglaciations. The pattern of increasing hydrothermal activity with increasing sea level is somewhat counterintuitive to the existing predictions of the sea level influence on mid-ocean ridges. Decreasing sea level is expected to increase decompression melting leading to greater melt production (Crowley et al., 2015; Huybers and Langmuir, 2009; Lund and Asimow, 2011). Previous interpretations of hydrothermal records have suggested that the deglacial peak in hydrothermal activity may lag the glacial sea level low stand by 5–10 kyr (Lund et al., 2016), since a delay between the sea level forcing and magmatic production, CO_2 release, and hydrothermal response is highly probable (Burley and Katz, 2015; Huybers and Langmuir, 2017). A much longer or variable lag could also be invoked, with an older triggering event of the sea level drop associated with glacial inception. A 60–100 kyr delay in the hydrothermal response to the gradual sea level decline associated with glaciation might account for the relatively long-lived hydrothermal response during the subsequent interglacial period.

The long record from the JdFR may help provide some constraints for both the potential lag duration and the threshold for sea level forcing to have an effect on hydrothermal activity (Fig. 10). Hydrothermal peaks occur during Termination I (∼10–20 ka), Termination II (128–138 ka), and Termination V (∼425–435 ka), but not during Termination III (∼240–250 ka) or

Termination IV (330–340 ka). Sea level generally declines slowly throughout 10 s of 1000 s of years of glaciation, but the largest amplitude sea level fall (>10 m/kyr) tends to occur during the initial glacial cooling (Grant et al., 2014). The terminations that contain hydrothermal peaks are all preceded by intense glacial periods (MIS2, MIS6, and MIS12), as defined by their heavy benthic oxygen isotopes (Lisiecki and Raymo, 2005). These glacial periods all contain abrupt sea level drops of >10 m/kyr, while the milder glacial periods (MIS8 and MIS10) do not achieve sea level declines that exceed 10 m/kyr. This correlation between sea level decline and enhanced deglacial hydrothermal activity may indicate a threshold effect, in which hydrothermal responses will only be triggered following sea level drops that exceed ∼10 m/kyr, which occur only in the most extreme glacial periods. Once triggered, the hydrothermal response manifests after some lag, the duration of which would depend upon the mantle dynamics of the ridge (Crowley et al., 2015). At this time, there is currently no definitive evidence to link the deglacial hydrothermal peaks to any specific preceding sea level drop, and in some cases, i.e. the last deglaciation, there are multiple potential triggering events that would entail lags ranging from 20 kyr to 100 kyr. While this threshold hypothesis explains the absence of hydrothermal peaks in TIII and TIV, it may require corollary mechanisms to capture the full complexity of hydrothermal systems, including the timing and amplitude of hydrothermal peaks.

Alternatively, the hydrothermal activity that peaks during terminations may be responding to the coincident increase in sea level. Hydrothermal fluids are generated by the percolation of seawater through fractures in the basement rock that facilitate chemical reactions with the basalt at high temperatures. The aforementioned relationship between sea level fall and hydrothermal activity is predicated on an increase in magmatic volume and/or magmatic temperature. Instead, hydrothermal activity could be enhanced by a greater flux of seawater through the basement rock, for example, during periods of tectonic activity that generate extensive fracture networks. On the northern East Pacific Rise, for example, hydrothermal activity is more intense in the tectonized portions of the ridge than in the more magmatically dominated regions (Baker et al., 2001), and this spatial pattern is attributed to a faulting control on the incidence of hydrothermal activity (Baker et al., 2001). Deglacial increases in the seawater overburden might also contribute to enhanced fluid–rock interactions. Although the exact mechanism driving the propagation of sea level forcing into hydrothermal systems is not yet fully characterized, it is clear that multiple mid-ocean ridges are capturing a global signal of changes in hydrothermal flux that coincide with periods of climate change. Future work generating long hydrothermal records from other ridges may help to provide insight into the mechanisms behind the responsiveness, manifestation, and evolution of sea level forcing on mid ocean ridge systems.

7. Conclusions

The hydrothermal records presented here provide the longest orbitally resolved reconstructions of hydrothermal activity currently available. Elemental flux records of Fe_H, Mn_H, and Cu_H from the Cleft Segment of the Juan de Fuca Ridge allow the investigation of both proxy robustness and temporal variability. Hydrothermal deposition is a persistent feature of sedimentation along the ridge. There is a general decline in hydrothermal Fe deposition over the past 500 ka, potentially related to the diminishing influence of the Cobb hotspot on the magmatic center of the JdFR over time. Furthermore, Fe fluxes and global sea level are approximately in-phase over the last two glacial cycles, suggesting higher hydrothermal deposition during interglacial periods. Mn is found to be an unreliable hydrothermal index for the Juan de Fuca Ridge as it may

be susceptible to changes in redox conditions in the sediment, Cu fluxes are characterized by high-frequency events that may be linked to changes in vent temperature related to increased magmatic production during glacial periods. The hydrothermal history of the Juan de Fuca Ridge is consistent with previously published records from the Mid-Atlantic Ridge and the East Pacific Rise indicating a spike in hydrothermal deposition during the last deglaciation as well as the penultimate deglaciation. However, the Juan de Fuca Ridge data suggest that these deglacial peaks may accompany a transition to prolonged higher hydrothermal activity continuing into the ensuing interglacial periods at this location.

Finally, this work identifies several key lines of research to be pursued in future work. One direction is that variability in the composition of lithogenic material may have a considerable influence on the isolation and interpretation of hydrothermal fluxes, and further examination of this variability may improve the accuracy and interpretation of future hydrothermal reconstructions. Another is that the relationship between sea level, melt supply, and hydrothermal activity is poorly understood. Complex interactions between the size of the magma chamber, the depth of hydrothermal irrigation, and the temperature of the fluid–rock interactions may all affect the timing, magnitude, and composition of the hydrothermal record of sea level effects on mid-ocean ridges. Coupled geophysical and geochemical modeling of hydrothermal systems will provide more tailored expectations for how hydrothermal systems respond to sea level change.

Acknowledgements

Appendix A. Supplementary material

Supplementary material related to this article can be found online at http://dx.doi.org/10.1016/j.epsl.2017.09.006.

References

Bacon, M.P., 1984. Glacial to interglacial changes in carbonate and clay sedimentation in the Atlantic Ocean estimated from ^{230}Th measurements. Isot. Geosci. 2, 97–111.

Baker, E.T., 1994. A 6-year time series of hydrothermal plumes over the Cleft segment of the Juan de Fuca Ridge. J. Geophys. Res. 99, 4889–4904.

Baker, E.T., Cormier, M.-H., Langmuir, C.H., Zavala, K., 2001. Hydrothermal plumes along segments of contrasting magmatic influence, 15°20′–18°30′N, East Pacific Rise: influence of axial faulting. Geochem. Geophys. Geosyst. 2, 2000GC000165. http://dx.doi.org/10.1002/2014GC005684.Key.

Baker, E.T., Hammond, S.R., 1992. Hydrothermal venting and the apparent magmatic budget of the Juan de Fuca Ridge. J. Geophys. Res. 97, 3443–3456. http://dx.doi.org/10.1029/91JB02671.

Baker, E.T., Lavelle, J.W., Massoth, G.J., 1985. Hydrothermal particle plumes over the southern Juan de Fuca Ridge. Nature 316, 342–344. http://dx.doi.org/10.1038/316342a0.

Baker, E.T., Massoth, G.J., Feely, R.A., 1987. Cataclysmic hydrothermal venting on the Juan de Fuca ridge. Nature 329, 149–151.

Beaulieu, S.E., Baker, E.T., German, C.R., Maffei, A., 2013. An authoritative global database for active submarine hydrothermal vent fields. Geochem. Geophys. Geosyst. 14, 4892–4905. http://dx.doi.org/10.1002/2013GC004998.

Berger, W.H., Finkel, R.C., Killingley, J.S., Marchig, V., 1983. Glacial-Holocene transition in deep-sea sediments: manganese-spike in the east equatorial Pacific. Nature 303, 231–233.

Burley, J.M.A., Katz, R.F., 2015. Variations in mid-ocean ridge CO_2 emissions driven by glacial cycles. Earth Planet. Sci. Lett. 426, 246–258. http://dx.doi.org/10.1016/j.epsl.2015.06.031.

Butterfield, D.A., Jonasson, I.R., Massoth, G.J., Feely, R.A., Roe, K.K., Embley, R.E., Holden, J.F., McDuff, R.E., Lilley, M.D., Delaney, J.R., 1997. Seafloor eruptions and evolution of hydrothermal fluid chemistry. Philos. Trans. R. Soc. Lond. 355, 369–386.

Butterfield, D.A., Massoth, G.J., 1994. Geochemistry of north Cleft segment vent fluids: temporal changes in chlorinity and their possible relation to recent volcanism. J. Geophys. Res. 99, 4951–4968. http://dx.doi.org/10.1029/93JB02798.

Carbotte, S.M., Nedimović, M.R., Canales, J.P., Kent, G.M., Harding, A.J., Marjanović, M., 2008. Variable crustal structure along the Juan de Fuca Ridge: influence of on-axis hot spots and absolute plate motions. Geochem. Geophys. Geosyst. 9. http://dx.doi.org/10.1029/2007GC001922.

Chakraborty, P., Sander, S.G., Jayachandran, S., Nath, B.N., Nagaraju, G., Chennuri, K., Vudamala, K., Lathika, N., Mascarenhas-pereira, M.B.L., 2014. Fate of copper complexes in hydrothermally altered deep-sea sediments from the Central Indian Ocean Basin. Environ. Pollut. 194, 138–144. http://dx.doi.org/10.1016/j.envpol.2014.07.012.

Charlou, J.L., Donval, J.P., Douville, E., Jean-Baptiste, P., Radford-Knoery, J., Fouquet, Y., Dapoigny, A., Stievenard, M., 2000. Compared geochemical signatures and the evolution of Menez Gwen (35°50N) and Lucky Strike (37°17N) hydrothermal fluids, south of the Azores Triple Junction on the Mid-Atlantic Ridge. Chem. Geol. 171, 49–75. http://dx.doi.org/10.1016/S0009-2541(00)00244-8.

Costa, K.M., McManus, J.F., 2017. Efficacy of ^{230}Th normalization in sediments from the Juan de Fuca Ridge, northeast Pacific Ocean. Geochim. Cosmochim. Acta 197, 215–225. http://dx.doi.org/10.1016/j.gca.2016.10.034.

Costa, K.M., McManus, J.F., Boulahanis, B., Carbotte, S.M., Winckler, G., Huybers, P., Langmuir, C.H., 2016. Sedimentation, stratigraphy and physical properties of sediment on the Juan de Fuca Ridge. Mar. Geol. 380, 163–173.

Cowen, J.P., Massoth, G.J., Baker, E.T., 1986. Bacterial scavenging of Mn and Fe in a mid- to far-field hydrothermal particle plume. Nature 322, 169–171.

Crerar, D.A., Barnes, H.L., 1976. Ore solution chemistry V. Solubilities of chalcopyrite, chalcocite assemblages in hydrothermal solutions at 22° to 350°C. Econ. Geol. 71, 772–794.

Crowley, J.W., Katz, R.F., Huybers, P., Langmuir, C.H., Park, S.H., 2015. Glacial cycles drive variations in the production of oceanic crust. Science 80 (347), 1237–1240. http://dx.doi.org/10.1126/science.1261508.

Desonie, D.L., Duncan, R.A., 1990. The Cobb–Eickelberg seamount chain: hotspot volcanism with mid-ocean ridge basalt affinity. J. Geophys. Res. 95, 12697–12711.

Dick, G.J., Clement, B.G., Webb, S.M., Fodrie, F.J., Bargar, J.R., Tebo, B.M., 2009. Enzymatic microbial Mn(II) oxidation and Mn biooxide production in the Guyamas Basin deep-sea hydrothermal plume. Geochim. Cosmochim. Acta 73, 6517–6530.

Dixon, J.E., Clague, D.A., Eissen, J.-P., 1986. Gabbroic zenoliths and host ferrobasalt from the Southern Juan de Fuca Ridge. J. Geophys. Res. 91, 3795–3820.

Douville, E., Charlou, J.L., Oelkers, E.H., Bienvenu, P., Jove Colon, C.F., Donval, J.P., Fouquet, Y., Prieur, D., Appriou, P., 2002. The rainbow vent fluids (36°14′N, MAR): the influence of ultramafic rocks and phase separation on trace metal content in Mid-Atlantic Ridge hydrothermal fluids. Chem. Geol. 184, 37–48. http://dx.doi.org/10.1016/S0009-2541(01)00351-5.

Dunk, R.M., Mills, R.A., 2006. The impact of oxic alteration on plume-derived transition metals in ridge flank sediments from the East Pacific Rise. Mar. Geol. 229, 133–157. http://dx.doi.org/10.1016/j.margeo.2006.03.007.

Edmonds, H.N., German, C.R., 2004. Particle geochemistry in the Rainbow hydrothermal plume, Mid-Atlantic Ridge. Geochim. Cosmochim. Acta 68, 759–772. http://dx.doi.org/10.1016/S0016-7037(03)00498-8.

Embley, R.W., Chadwick, W.W.J., 1994. Volcanic and hydrothermal processes associated with a recent phase of seafloor spreading at the northern Cleft segment, Juan de Fuca Ridge. J. Geophys. Res., Solid Earth 99, 4741–4760. http://dx.doi.org/10.1029/93JB02038.

Feely, R.A., Lewison, M., Massoth, G.J., Robert-Baldo, G., Lavelle, J.W., Byrne, R.H., Von Damm, K.L., Curl Jr., H.C., 1987. Composition and Dissolution of Black Smoker Particulates From Active Vents on the Juan de Fuca Ridge. J. Geophys. Res. 92, 11347–11363.

Feely, R.A., Massoth, G.J., Trefry, J.H., Baker, E.T., Paulson, A.J., Lebon, G.T., 1994. Composition and sedimentation of hydrothermal plume particles from north Cleft segment, Juan de Fuca Ridge. J. Geophys. Res. 99, 4985–5006. http://dx.doi.org/10.1029/93JB02509.

Feely, R.A., Trefry, J.H., Massoth, G.J., Metz, S., 1990. A comparison of the scavenging of phosphorous and arsenic from seawater by hydrothermal iron oxyhydroxides in the Atlantic and Pacific Oceans. Deep Sea Res. 38, 617–623.

Ferguson, D.J., Li, Y., Langmuir, C.H., Costa, K.M., McManus, J.F., Huybers, P., Carbotte, S.M., 2017. A 65 k.y. time series from sediment-hosted glasses reveals rapid transitions in ocean ridge magmas. Geology, 4–7. http://dx.doi.org/10.1130/G38752.1.

Ferrat, M., Weiss, D.J., Strekopytov, S., Dong, S., Chen, H., Najorka, J., Sun, Y., Gupta, S., Tada, R., Sinha, R., 2011. Improved provenance tracing of Asian dust sources using rare earth elements and selected trace elements for palaeomonsoon studies on the eastern Tibetan Plateau. Geochim. Cosmochim. Acta 75, 6374–6399. http://dx.doi.org/10.1016/j.gca.2011.08.025.

Findlay, A.J., Gartman, A., Shaw, T.J., Luther, G.W., 2015. Trace metal concentration and partitioning in the first 1.5 m of hydrothermal vent plumes along the Mid-Atlantic Ridge: TAG, Snakepit, and Rainbow. Chem. Geol. 412, 117–131. http://dx.doi.org/10.1016/j.chemgeo.2015.07.021.

Fitzsimmons, J.N., John, S.G., Marsay, C.M., Hoffman, C.L., Nicholas, S.L., Toner, B.M., German, C.R., Sherrell, R.M., 2017. Iron persistence in a distal hydrothermal plume supported by dissolved-particulate exchange. Nat. Geosci. 10, 195–201. http://dx.doi.org/10.1038/NGEO2900.

Francois, R., Frank, M., Rutgers van der Loeff, M., Bacon, M.P., 2004. ^{230}Th normalization: an essential tool for interpreting sedimentary fluxes during the late Quaternary. Paleoceanography 19, PA1018. http://dx.doi.org/10.1029/2003PA000939.

Frank, M., Eisenhauer, A., Bonn, W.J., Walter, P., Grobe, H., Kubik, P.W., Dittrich-Hannen, B., Mangini, A., 1995. Sediment redistribution versus paleoproductivity change: Weddell Sea margin sediment stratigraphy and biogenic particle flux of the barium profiles. Earth Planet. Sci. Lett. 136, 559–573.

Frank, M., Eisenhauer, A., Kubik, P.W., Dittrich-Hannen, B., Segl, M., Mangini, A., 1994. Beryllium-10, thorium-230, and protactinium-231 in Galapagos microplate sediments: implications of hydrothermal activity and paleoproductivity changes during the last 100,000 years. Paleoceanography 9, 559–578.

Froelich, P.N., Klinkhammer, G.P., Bender, M.L., Luedtke, N.A., Heath, G.R., Cullen, D., Dauphin, P., Hammond, D., Hartman, B., Maynard, V., 1979. Early oxidation of organic matter in pelagic sediments of the eastern equatorial Atlantic: suboxic diagenesis. Geochim. Cosmochim. Acta 43, 1075–1090.

Gartman, A., Findlay, A.J., Luther, G.W., 2014. Nanoparticulate pyrite and other nanoparticles are a widespread component of hydrothermal vent black smoker emissions. Chem. Geol. 366, 32–41. http://dx.doi.org/10.1016/j.chemgeo.2013.12.013.

German, C.R., Bourles, D.L., Brown, E.T., Hergt, J., Colley, S., Higgs, N.C., Ludford, E.M., Nelsen, T.A., Feely, R.A., Raisbeck, G., Yiou, F., 1997. Hydrothermal scavenging on the Juan de Fuca Ridge: ^{230}Th$_{xs}$, ^{10}Be, and REEs in ridge-flank sediments. Geochim. Cosmochim. Acta 61, 4067–4078.

German, C.R., Colley, S., Palmer, M.R., Khripounoff, A., Klinkhammer, G.P., 2002. Hydrothermal plume-particle fluxes at 13°N on the East Pacific Rise. Deep-Sea Res., Part 1, Oceanogr. Res. Pap. 49, 1921–1940. http://dx.doi.org/10.1016/S0967-0637(02)00086-9.

German, C.R., Fleer, A.P., Bacon, M.P., Edmond, J.M., 1991. Hydrothermal scavenging at the Mid-Atlantic Ridge: radionuclide distributions. Earth Planet. Sci. Lett. 105, 170–181. http://dx.doi.org/10.1016/0012-821X(91)90128-5.

German, C.R., Thurnherr, A.M., Knoery, J., Charlou, J.L., Jean-Baptiste, P., Edmonds, H.N., 2010. Heat, volume and chemical fluxes from submarine venting: a synthesis of results from the Rainbow hydrothermal field, 36°N MAR. Deep-Sea Res., Part 1, Oceanogr. Res. Pap. 57, 518–527. http://dx.doi.org/10.1016/j.dsr.2009.12.011.

Goldberg, E.D., Arrhenius, G.O.S., 1958. Chemistry of Pacific pelagic sediments. Geochim. Cosmochim. Acta 13, 153–212.

Grant, K.M., Rohling, E.J., Ramsey, C.B., Cheng, H., Edwards, R.L., Florindo, F., Heslop, D., Marra, F., Roberts, A.P., Tamisiea, M.E., Williams, F., 2014. Sea-level variability over five glacial cycles. Nat. Commun. 5, 5076. http://dx.doi.org/10.1038/ncomms6076.

Huybers, P., Langmuir, C., 2009. Feedback between deglaciation, volcanism, and atmospheric CO_2. Earth Planet. Sci. Lett. 286, 479–491. http://dx.doi.org/10.1016/j.epsl.2009.07.014.

Huybers, P., Langmuir, C., Katz, R.F., Ferguson, D., Proistosescu, C., Carbotte, S., 2016. Comment on "Sensitivity of seafloor bathymetry to climate-driven fluctuations in mid-ocean ridge magma supply". Science 352 (80), 1405b. http://dx.doi.org/10.1126/science.aae0451.

Huybers, P., Langmuir, C.H., 2017. Delayed CO_2 emissions from mid-ocean ridge volcanism as a possible cause of late-Pleistocene glacial cycles. Earth Planet. Sci. Lett. 457, 238–249. http://dx.doi.org/10.1016/j.epsl.2016.09.021.

Jacobel, A.W., McManus, J.F., Anderson, R.F., Winckler, G., 2017. Climate-related response of dust flux to the central equatorial Pacific over the past 150 kyr. Earth Planet. Sci. Lett. 457, 160–172. http://dx.doi.org/10.1016/j.epsl.2016.09.042.

James, R.H., Elderfield, H., Palmer, M.R., 1995. The chemistry of hydrothermal fluids from the Broken Spur site, 29°N Mid-Atlantic ridge. Geochim. Cosmochim. Acta 59, 651–659.

Johnson, D.A., Johnson, T.C., 1970. Sediment redistribution by bottom currents in the central Pacific. Deep Sea Res. 17, 157–169. http://dx.doi.org/10.1016/0011-7471(70)90094-X.

Karsten, J.L., Delaney, J.R., 1989. Hot spot-ridge crest convergence in the northeast Pacific. J. Geophys. Res. 94, 700–712. http://dx.doi.org/10.1029/JB094iB01p00700.

Kienast, S.S., Kienast, M., Mix, A.C., Calvert, S.E., François, R., 2007. Thorium-230 normalized particle flux and sediment focusing in the Panama Basin region during the last 30,000 years. Paleoceanography 22. http://dx.doi.org/10.1029/2006PA001357.

Klevenz, V., Bach, W., Schmidt, K., Hentscher, M., Koschinsky, A., Petersen, S., 2012. Geochemistry of vent fluid particles formed during initial hydrothermal fluid-seawater mixing along the Mid-Atlantic Ridge. Geochem. Geophys. Geosyst. 12, 1–23. http://dx.doi.org/10.1029/2011GC003704.

Kuhn, T., Burger, H., Castradori, D., Halbach, P., 2000. Volcanic and hydrothermal history of ridge segments near the Rodrigues Triple Junction (Central Indian Ocean) deduced from sediment geochemistry. Mar. Geol. 169, 391–409. http://dx.doi.org/10.1016/S0025-3227(00)00080-3.

Kyte, F.T., Leinen, M., Ross Heath, G., Zhou, L., 1993. Cenozoic sedimentation history of the central North Pacific: inferences from the elemental geochemistry of core LL44-GPC3. Geochim. Cosmochim. Acta 57, 1719–1740. http://dx.doi.org/10.1016/0016-7037(93)90109-A.

Lisiecki, L.E., Raymo, M.E., 2005. A Pliocene–Pleistocene stack of 57 globally distributed benthic δ^{18}O records. Paleoceanography 20, PA1003. http://dx.doi.org/10.1029/2004PA001071.

Lund, D.C., Asimow, P.D., 2011. Does sea level influence mid-ocean ridge magmatism on Milankovitch timescales? Geochem. Geophys. Geosyst. 12, 149–151. http://dx.doi.org/10.1029/2011GC003693.

Lund, D.C., Asimow, P.D., Farley, K.A., Rooney, T.O., Seeley, E., Jackson, E.W., Durham, Z.M., 2016. Enhanced East Pacific Rise hydrothermal activity during the last two glacial terminations. Science 80 (351), 478–482. http://dx.doi.org/10.1126/science.aad4296.

Lyle, M.W., Owen, R.M., Leinen, M., 1986. History of hydrothermal sedimentation at the East Pacific Rise, 19°S. Init. Rep. Deep Sea Drill. Proj. 92, 585–596. http://dx.doi.org/10.1017/CBO9781107415324.004.

Massoth, G.J., Baker, E.T., Lupton, J.E., Feely, R.A., Butterfield, D.A., Von Damm, K.L., Roe, K.K., Lebon, G.T., 1994. Temporal and spatial variability of hydrothermal manganese and iron at Cleft segment, Juan de Fuca Ridge. J. Geophys. Res. 99, 4905–4923.

McManus, J.F., Anderson, R.F., Broecker, W.S., Fleisher, M.Q., Higgins, S.M., 1998. Radiometrically determined sedimentary fluxes in the sub-polar North Atlantic during the last 140,000 years. Earth Planet. Sci. Lett. 155, 29–43.

Mekik, F., 2014. Radiocarbon dating of planktonic foraminifer shells: a cautionary tale. Paleoceanography 29, 13–29. http://dx.doi.org/10.1002/2013PA002532.

Metz, S., Trefry, J.H., 2000. Chemical and mineralogical influences on concentrations of trace metals in hydrothermal fluids. Geochim. Cosmochim. Acta 64, 2267–2279. http://dx.doi.org/10.1016/S0016-7037(00)00354-9.

Middleton, J.L., Langmuir, C.H., Mukhopadhyay, S., McManus, J.F., Mitrovica, J.X., 2016. Hydrothermal iron flux variability following rapid sea level changes. Geophys. Res. Lett. 43, 1–9. http://dx.doi.org/10.1002/2016GL068408.Received.

Mills, R.A., Taylor, S.L., Pälike, H., Thomson, J., 2010. Hydrothermal sediments record changes in deep water oxygen content in the SE Pacific. Paleoceanography 25, PA4226. http://dx.doi.org/10.1029/2010PA001959.

Murray, R.W., Leinen, M., Isern, A.R., 1993. Biogenic flux of al to sediment in the Central Equatorial Pacific Ocean: evidence for increased productivity during Glacial periods. Paleoceanography 8, 651–670. http://dx.doi.org/10.1029/93pa02195.

Murray, R.W., Miller, D.J., Kryc, K.A., 2000. Analysis of major and trace elements in rocks, sediments, and interstitial waters by inductively coupled plasma-atomic emission spectrometry (ICP-AES). ODP Tech. Note.

Normark, W.R., Morton, J.L., Koski, R.A., Clague, D.A., Delaney, J.R., 1983. Active hydrothermal vents and sulfide deposits on the southern, Juan de Fuca Ridge. Geology 11, 158.

Olive, J.-A., Behn, M.D., Ito, G., Buck, W.R., Escartín, J., Howell, S., 2015. Sensitivity of seafloor bathymetry to climate-driven fluctuations in mid-ocean ridge magma supply. Science 80 (350), 310–313.

Olive, J.-A., Behn, M.D., Ito, G., Buck, W.R., Escartín, J., Howell, S., 2016a. Response to Comment on "Sensitivity of seafloor bathymetry to climate-driven fluctuations in mid-ocean ridge magma supply". Science 80, 229c. http://dx.doi.org/10.1126/science.aae0451.

Olive, J.-A., Behn, M.D., Ito, G., Buck, W.R., Escartín, J., Howell, S., 2016b. Response to Comment on "Sensitivity of seafloor bathymetry to climate-driven fluctuations in mid-ocean ridge magma supply". Science 352 (80), 1405c. http://dx.doi.org/10.1126/science.aae0451.

Pavia, F., Anderson, R., Vivancos, S., Fleisher, M., Lam, P., Lu, Y., Cheng, H., Zhang, P., Edwards, R.L., 2017. Intense hydrothermal scavenging of ^{230}Th and ^{231}Pa in the deep Southeast Pacific. Mar. Chem. http://dx.doi.org/10.1016/j.marchem.2017.08.003.

Plank, T., 2014. The Chemical Composition of Subducting Sediments. In: The Crust. Treatise Geochemistry (Second Ed.), vol. 4, pp. 607–629.

Resing, J.A., Sedwick, P.N., German, C.R., Jenkins, W.J., Moffett, J.W., Sohst, B.M., Tagliabue, A., 2015. Basin-scale transport of hydrothermal dissolved metals across the South Pacific Ocean. Nature 523, 200–203. http://dx.doi.org/10.1038/nature14577.

Rickard, D., Cowper, M., 1994. Kinetics and mechanisms of chalcopyrite formation from Fe(II) disulphide in aqueous solution (<200°C). Geochim. Cosmochim. Acta 58, 3795–3802.

Rousseau, R.M., Willis, J.P., Duncan, A.R., 1996. Practical XRF calibration procedures for major and trace elements. X-Ray Spectrom. 25, 179–189. http://dx.doi.org/10.1002/(SICI)1097-4539(199607)25:4<179::AID-XRS162>3.0.CO;2-Y.

Rudnicki, M.D., 1995. Particle formation, fallout and cycling within the buoyant and non-buoyant plume above the TAG vent field. Geol. Soc. (Lond.) Spec. Publ. 87, 387–396. http://dx.doi.org/10.1144/GSL.SP.1995.087.01.30.

Ruhlemann, C., Frank, M., Hale, W., Mangini, A., Mulitza, S., Muller, P.J., Wefer, G., 1996. Late Quaternary productivity changes in the western equatorial Atlantic: evidence from ^{230}Th-normalized carbonate and organic carbon accumulation rates. Mar. Geol. 135, 127–152. http://dx.doi.org/10.1016/S0025-3227(96)00048-5.

Rusakov, V.Y., 2007. Comparative analysis of the mineral and chemical compositions of black smoker smoke at the TAG and broken spur hydrothermal fields, mid-atlantic ridge. Geochem. Int. 45, 766–785. http://dx.doi.org/10.1134/S0016702907070063.

Sander, S.G., Koschinsky, A., 2011. Metal flux from hydrothermal vents increased by organic complexation. Nat. Geosci. 4, 145–150. http://dx.doi.org/10.1038/ngeo1088.

Schaller, T., Morford, J.L., Emerson, S., Feely, R.A., 2000. Oxyanions in metalliferous sediments: tracers for paleoseawater metal concentrations? Geochim. Cosmochim. Acta 64, 2243–2254.

Seewald, J.S., Seyfried, W.E., 1990. The effect of temperature on metal mobility in subseafloor hydrothermal systems: constrains from basalt alteration experiments. Earth Planet. Sci. Lett., 388–403.

Seyfried, W.E., Ding, K., 1995. Phase equilibria in subseafloor hydrothermal systems: a review of the role of redox, temperature, pH and dissolved Cl on the chemistry of hot spring fluids at mid-ocean ridges. In: Humphris, S.E., Zierenberg, R.A., Mullineaux, L.S., Thomson, R.E. (Eds.), Seafloor Hydrothermal Systems, Physical, Chemical, Biological, and Geological Interactions. American Geophysical Union, Washington, D.C.

Seyfried, W.E., Seewald, J.S., Berndt, M.E., Ding, K., Foustoukos, D.I., 2003. Chemistry of hydrothermal vent fluids from the Main Endeavour Field, northern Juan de Fuca Ridge: geochemical controls in the aftermath of June 1999 seismic events. J. Geophys. Res. 108, 2429. http://dx.doi.org/10.1029/2002JB001957.

Shimmield, G.B., Price, N.B., 1988. The scavenging of U, ^{230}Th, and ^{231}Pa during pulsed hydrothermal activity at 20°S, East Pacific Rise. Geochim. Cosmochim. Acta 52, 669–677.

Taylor, S.R., McLennan, S.M., 1995. The geochemical evolution of the continental crust. Rev. Geophys., 241–265.

Tebo, B.M., Bargar, J.R., Clement, B.G., Dick, G.J., Murray, K.J., Parker, D., Verity, R., Webb, S.M., 2004. Biogenic manganese oxides: properties and mechanisms of formation. Annu. Rev. Earth Planet. Sci. 32, 287–328.

Thomson, J., Colley, S., Anderson, R.F., Cook, G.T., MacKenzie, A.B., Harkness, D.D., 1993. Holocene sediment fluxes in the Northeast Atlantic from ^{230}Th$_{excess}$ and radiocarbon measurements. Paleoceanography 8, 631–650.

Tolstoy, M., 2015. Mid-ocean ridge eruptions as a climate valve. Geophys. Res. Lett. 2014GL063015. http://dx.doi.org/10.1002/2014GL063015.

Tolstoy, M., 2016. Comment on "Sensitivity of seafloor bathymetry to climate-driven fluctuations in mid-ocean ridge magma supply". Science 80, 229b. http://dx.doi.org/10.1126/science.aae0451.

Trefry, J.H., Butterfield, D.B., Metz, S., Massoth, G.J., Trocine, R.P., Feely, R.A., 1994. Trace metals in hydrothermal solution from Cleft segment on the southern Juan de Fuca Ridge. J. Geophys. Res. 99, 4925–4935.

Von Damm, K.L., 1990. Seafloor hydrothermal activity: black smoker chemistry and chimneys. Annu. Rev. Earth Planet. Sci. 18, 173–204.

Von Damm, K.L., Bischoff, J.L., 1987. Chemistry of hydrothermal solutions from the southern Juan de Fuca Ridge. J. Geophys. Res. 92, 11334. http://dx.doi.org/10.1029/JB092iB11p11334.

Von Damm, K.L., Bray, A.M., Buttermore, L.G., Oosting, S.E., 1998. The geochemical controls on vent fluids from the Lucky Strike vent field, Mid-Atlantic Ridge. Earth Planet. Sci. Lett. 160, 521–536. http://dx.doi.org/10.1016/S0012-821X(98)00108-3.

Von Damm, K.L., Edmond, J.M., Grant, B., Measures, C.I., Walden, B., Weiss, R.F., 1985. Chemistry of submarine hydrothermal solutions at 21°N, East Pacific Rise. Geochim. Cosmochim. Acta 49, 2197–2220.

Whetten, J., Kelley, J., Hanson, L., 1969. Characteristics of Columbia River sediment and sediment transport. J. Sediment. Petrol. 39, 1149–1166.

White, S.M., 1970. Mineralogy and geochemistry of continental shelf sediments off the Washington-Oregon coast. J. Sediment. Petrol. 40, 38–54.

Wilson, D.S., 1993. Confidence intervals for motion and deformation of the Juan de Fuca plate. J. Geophys. Res. 98, 16053–16071.

Winckler, G., Anderson, R.F., Fleisher, M.Q., McGee, D., Mahowald, N., 2008. Covariant glacial–interglacial dust fluxes in the equatorial Pacific and Antarctica. Science 320, 93–96. http://dx.doi.org/10.1126/science.1150595.

Yücel, M., Gartman, A., Chan, C.S., Luther, G.W., 2011. Hydrothermal vents as a kinetically stable source of iron-sulphide-bearing nanoparticles to the ocean. Nat. Geosci. 4, 367–371. http://dx.doi.org/10.1038/ngeo1148.